A Data-driven Approach for Generalizing the Laminar Kinetic Energy Model for Separation and Bypass Transition in Low- and High-pressure Turbines

Yuan Fang[*†]
Department of Mechanical Engineering
University of Melbourne, VIC, 3010, Australia
Email: yuanfang1@student.unimelb.edu.au

Yaomin Zhao

Center for Applied Physics
and Technology, HEDPS
College of Engineering
Peking University, Beijing 100871, China
Email: yaomin.zhao@pku.edu.cn

Harshal D. Akolekar

Department of Mechanical Engineering
Indian Institute of Technology,
Jodhpur, 324037, India
University of Melbourne,
VIC, 3010, Australia
Email: harshal.akolekar@iitj.ac.in

Andrew S. H. Ooi
Richard D. Sandberg
Department of Mechanical Engineering
University of Melbourne,
VIC, 3010, Australia
Email: a.ooi@unimelb.edu.au
richard.sandberg@unimelb.edu.au

Roberto Pacciani
Michele Marconcini
Department of Industrial Engineering
University of Florence,
50139 Florence, Italy
Email: roberto.pacciani@unifi.it
michele.marconcini@unifi.it

ABSTRACT

[*]Address all correspondence related to ASME style format and figures to this author.
[†]Address all correspondence for other issues to this author.

No common laminar kinetic energy (LKE) transition model has to date been able to predict both separation-induced and bypass transition, both phenomena commonly found in low-pressure turbines (LPT) and high-pressure turbines (HPT). Here, a data-driven approach is adopted to develop a more general LKE transition model suitable for both transition modes. To achieve this, two strategies are adopted. The first is to extend the computational fluid dynamics (CFD)-driven model training framework for simultaneously training models on multiple turbine cases, subject to multiple objectives. By increasing the training data set, different transition modes can be considered. The second strategy employed is the use of a newly derived set of local non-dimensionalized variables as training inputs to reduce the search space. Because one of the training turbine cases is characterized by strong unsteady effects, for the first time an unsteady solver is utilized during the CFD-Driven training, and the time-averaged results are used to calculate the cost function as part of the model development process. The results show that the data-driven models do perform better, in terms of their predictions of pressure coefficient, wall shear stress, and wake losses, than the baseline model. The models were then tested on two previously unseen testing cases, one at a higher Reynolds number and one with a different geometry. For both testing cases, stable solutions were obtained with results improved over the predictions using the baseline models.

NOMENCLATURE

$\boldsymbol{a}_{ij}$ Extra anisotropy stress

C_{ax} The axial chord

C_f Friction coefficient

C_p Pressure coefficient

f_i Trained functions in the transition model

g_i Trained functions in the extra anisotropy stress

H Shape factor

I_i Scalar invariants in extra anisotropic stress

J Objective function

k_l Laminar kinetic energy

k Turbulent kinetic energy

l_t Turbulence length scale, $l_t = \frac{\sqrt{k}}{\omega}$

Ma Mach number

P Production term

P_i Non-dimensional inputs to train the transition model

Q Quantity of interest

R Transfer term

Re Reynolds number

R_y wall-normal-distance Reynolds number, $R_y = \frac{\sqrt{k}y}{\nu}$

Tu_∞ Free-stream turbulence intensity

U velocity magnitude

$\boldsymbol{V}_{ij}$ Tensor basis in extra anisotropic stress

y wall distance

x, y Cartesian coordinates

$\boldsymbol{\delta}_{ij}$ Kronecker Delta

$\boldsymbol{s}_{ij}$, $\boldsymbol{\omega}_{ij}$ non-dimensional mean strain and rotation rate

$\boldsymbol{S}^*_{ij}$ Deviatoric strain rate $\boldsymbol{S}^*_{ij} = \boldsymbol{S}_{ij} - \frac{1}{3}\frac{\partial u_k}{\partial x_k}\delta_{ij}$

ϵ_l Dissipation term of laminar kinetic energy

ω Specific dissipation rate

μ_t turbulent dynamic viscosity

ν_t, ν turbulent and fluid kinematic viscosity

ρ Fluid density

Ω Vorticity magnitude

Ω^* Wake loss

$\boldsymbol{\tau}_{ij}$ Reynolds stress tensor

τ_w Wall shear stress

δ_Ω shear layer vorticity thickness

θ Boundary thickness

δ Momentum thickness

SUBSCRIPTS/SUPERSCRIPTS

l Laminar

k Turbulent

∞ Freestream

$truth$ The ground truth

ACRONYMS

LKE Laminar kinetic energy

TKE Turbulent kinetic energy

LPT Low-pressure turbine

HPT High-pressure turbine

CFD Computational fluid dynamics

(U)RANS (Unsteady) Reynolds averaged Navier-Stokes

DNS Direct Numerical Simulation

LES Large Eddy Simulation

ML Machine Learning

ANN artificial neural network

GPR Gaussian process regression

GEP Gene expression programming

FSTI Free-stream turbulence intensity

INTRODUCTION

The laminar-turbulent transition phenomenon plays a significant role in gas turbine engines. In gas turbines, transition is a major source of uncertainty regarding performance and long-term reliability, but accurately modeling the many paths of transition remains a major challenge. Since the turbulent heat transfer and aerodynamic loss resulting from transitional and turbulent flows are larger than for laminar flow, improved prediction of transition is essential. Such an improvement will contribute to the design of lighter and smaller engines [1], potentially leading to significant fuel savings and emission reductions [2].

High and low-pressure turbines, two key components in gas turbines, often undergo different modes of transition. Operating at high pressure and temperature conditions, the high-pressure turbine (HPT) blades are designed with a large leading edge to leave room for the cooling system in order to reduce the heat load [3]. Induced by the incoming high-amplitude free-stream turbulence flow, HPTs often undergo bypass transition. As the name suggests, this transition mode bypasses the initial two-dimensional instability phase of natural transition [3]. Streamwise elongated disturbances termed as streaks are induced in the laminar boundary layer. These streaks then break down and form turbulent spots [4]. Further downstream, the flow enters the low-pressure turbine (LPT) where the high-lift blades extract power to drive the propulsion device [1]. With the decreased Mach and Reynolds number of the flow, LPTs generally experience separation-induced transition. At the leading edge or downstream of the point of minimum pressure on the suction side, the laminar boundary layer may separate. Then transition occurs in the free shear layer and the turbulent flow may reattach to form a closed separation or might remain detached to cause an open separation [5]. These two transition modes need to be captured numerically in the initial design to accurately predict the heat load for an HPT and the aerodynamic loss for an LPT.

In the early design phase, (Unsteady) Reynolds Averaged Navier-Stokes ((U)RANS) are routinely used as they are significantly more cost-effective than high-fidelity simulations or experiments. However, (U)RANS employs both turbulence and transition models, which directly affects the accuracy of the predictions. The transition models can be broadly characterized into two categories, namely correlation-based and physical-based models [6]. The former type derives the onset and growth of transition from experimental correlations. A typical example is based on the concept of intermittency defined as the probability of a flow being turbulent at a certain location [5]. Various intermittency models have been proposed, from algebraic models including conditionally averaged flow equations [7] and streamwise algebraic transition models [8, 9], to intermittency transport models including local correlation-based ones [10, 11] and non-local ones [12]. These types of intermittency-based models are known to function well on bypass transition, but do not yield satisfactory results for separation-induced transition.

An alternative to correlation-based transition models is physical-based ones, focusing on modeling the physical flow structure during transition. As a prominent representative, the laminar kinetic energy (LKE), a concept originally proposed by Mayle and Schulz [13] models the laminar fluctuations in the pre-transition region of a boundary layer [6]. They formulated an LKE transport equation mimicking the turbulent transport process. In this model, the production of LKE is believed to be triggered by imposing fluctuating pressure forces. However, recent research has shown that the laminar fluctuation amplification comes from the conventional shear-stress/strain interaction [14], similar to the evolution of turbulent fluctuations, rather than from pressure diffusion [13]. Hence, Walters and Leylek [15, 16, 17] and Lardeau et al. [18] developed LKE models with a production term that is proportional to the square of the mean shear rate. In addition to that revision, they sensitized two production terms by using two sensors to activate the onset of steady natural and bypass transition, instead of using one production term as in Mayle and Schulz's model [13]. However, as their models have no specific terms for separation-induced transition, Pacciani et al. [19] proposed a new LKE production term to model transition in a separated state. This production structure was kept in their updated model with an additional equation for the turbulent indicator function associated with wake turbulence. Although good performance has been shown for single-type transition, no LKE model has to date been built that satisfactorily captures both bypass and separation-induced transition, due to their different physical regimes. Hence, a more general LKE transition model that performs well across different turbine configurations, with different transition paths and trailing-edge separation behavior, becomes the goal of this study.

A data-driven approach is adopted here due to the recent promising results for model development. Although considerable efforts have been put into machine learning (ML) assisted turbulence modeling, transition model development via ML has been much more limited. Duraisamy and Durbin [20] first attempted to construct the difference of the source and sink terms in an intermittency model for bypass transition using field inversion and machine learning methods, including an artificial neural network (ANN) and Gaussian process regression (GPR). Yang and Xiao [21] also employed this two-step method to model the first Tollmien-Schlichting mode of the characteristic time scale in the flow transition. Wu et al. [22] on the other hand reconstructed the whole transition intermittency factor by ANN and coupled it with a two-equation turbulence model. In order to obtain interpretable and explicit ML-trained models rather than black-box ones, Akolekar et al. [23, 24] used gene expression programming (GEP) to revise the production and transfer terms in the LKE transition model and include extra anisotropy stress terms in the $k-\omega$ turbulence model. An enhanced prediction was obtained in that study. However, only a single case, a T106A data set, was used for training and thus the models were only sensitized for one transition mode and their performance for other cases was not known.

To build a more general LKE transition model, in this study, two strategies are adopted in the previously used data-driven method [24]. The first is extending the original single-case multi-objective CFD-Driven training framework [25] to a multi-case training framework. Increasing the training data set to multiple configurations ensures that models are trained considering different transition modes. The second strategy is reducing the number of inputs for transition model training. Instead of the seven non-dimensional input parameters used in the previous work [24], we use a more concise parameter group that only consists of six inputs. This update reduces the search space of GEP, and thus speeds up the training convergence rate.

Another contribution that deserves attention is that an unsteady solver, for the first time, is utilized during CFD-Driven training. Among all the training cases, the HPT case experiencing bypass transition involves complicated physical phenomena such as shocks and strong vortex shedding. This causes numerical instability of the steady calculations and thus an unsteady solver is needed. A further benefit is gained as the present models trained in this way are expected to be applicable in both steady and unsteady RANS predictions.

The outline of this paper is as follows. In the methodology section, the baseline LKE transition model, the $k-\omega$ turbulence model, and their correction terms via the ML method are described. Then the multi-case multi-objectives CFD-Driven framework and the numerical setup of every turbine case are given. The trained models are then presented and analyzed and their performance discussed. The cross-validation results on two cases outside of training data sets are also discussed. The conclusion of this study is given in the last section.

METHODOLOGY

In this section, details of the mathematical model are given. Firstly, the formula of two terms in the baseline LKE transition model and their corresponding ML-trained components, and the nonlinear correction given by ML for the turbulence model are described. Then, the important components of the multi-case multi-objective CFD-Driven training framework including the input features and cost functions are introduced. Moreover, the (U)RANS formulations for the LPT and HPT configurations are briefly introduced.

Baseline models

LKE is identified as the pre-transition rise of the laminar fluctuating kinetic energy. The LKE baseline model used here was proposed by Pacciani *et al.*[19], constructed as follows:

$$\frac{Dk_l}{Dt} = P_l - \epsilon_l + \nu \nabla^2 k_l - R. \tag{1}$$

The unsteady and convection terms are on the left-hand side, and the production P_l, dissipation ($\epsilon_l = 2\mu k_l / y^2$), diffusion ($\nu \nabla^2 k_l$) and transfer terms R are on the right-hand side. As the name indicates, R represents the LKE transfer to turbulent kinetic energy (TKE) and is used to couple the transition model with the $k - \omega$ turbulence model:

$$\begin{aligned}
\frac{Dk}{Dt} &= P_k - \beta^* f_k k\omega + \frac{\partial}{\partial x_j}\left[(\nu + \delta_k \nu_t)\frac{\partial k}{\partial x_j}\right] + R, \\
\frac{D\omega}{Dt} &= \alpha \frac{\omega}{k} P_k - \beta^* \omega^2 + \frac{\partial}{\partial x_j}\left[(\nu + \delta_\omega \nu_t)\frac{\partial \omega}{\partial x_j}\right].
\end{aligned} \tag{2}$$

Among the terms in the LKE transition model, P_l controls the production of LKE and R adjusts the transfer of LKE to TKE. They are thus pertinent terms in the model and are identified to be the terms most likely to have a direct effect on the results. Hence, we will attempt to use ML to find improved formulations for P_l and R.

The production term P_l (see Eq.(3)) is formulated with the laminar eddy viscosity ν_l and the mean shear rate S. This is consistent with the latest research [6] indicating that the laminar fluctuations are amplified mainly due to the conventional shear-stress/strain interaction. The original laminar eddy-viscosity is constructed with an estimator of the shear-layer vorticity thickness δ_Ω, k_l and a constant C_1:

$$\begin{aligned}
&P_l = \nu_l S^2, \\
&\nu_l = C_1 \sqrt{k_l} \delta_\Omega, \\
&\delta_\Omega = \min\left(\frac{\Omega y^2}{U}, 2\right).
\end{aligned} \tag{3}$$

The transfer term R represents the process of LKE being transferred to the TKE. The original R term is

$$\begin{aligned}
&R = C_2 f_{t2} \omega k_l, \\
&f_{t2} = 1 - e^{\psi / C_3}, \\
&\psi = \max(\underbrace{R_y}_{\text{transition sensor}} - \underbrace{C_4}_{\text{threshold}}, 0), \\
&R_y = \sqrt{k} y / \nu.
\end{aligned} \tag{4}$$

As indicated by the construction of ψ in Eq. (4), the onset of transition is initiated when the flow feature sensor, the wall distance Reynolds number R_y, reaches the threshold value of C_4.

This baseline model has been reported to perform well for separation-induced transition [19]. If it is used to predict bypass transition, however, the coefficients in the LKE production and transfer

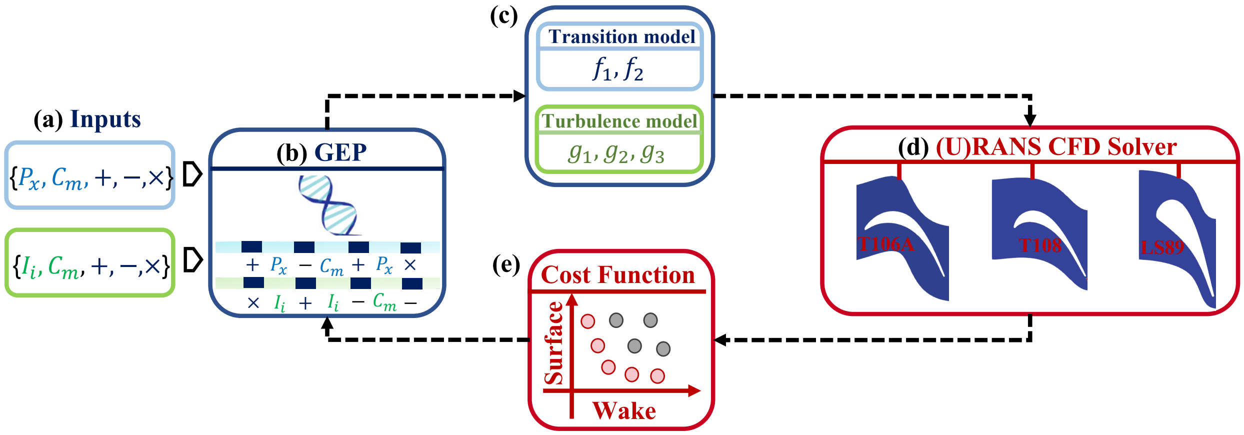

Fig. 1. The framework of multi-case multi-objective CFD-Driven training.

terms need to be considerably changed. For example, the coefficient in the LKE production term for an HPT needs to be 5 times larger than for the case of an LPT, while the coefficient in the transfer term needs to be 2 times smaller as found in preliminary baseline calculations. This enables the prediction of much larger LKE needed to accurately predict bypass transition.

The specific research problem now becomes clear: a data-driven methodology will be employed to obtain corrections to the LKE model that will include flow features that are sensitive to transition as inputs. The main outcome is to obtain a transition model that will give good predictions for both transition modes.

ML for model corrections

ML-trained model corrections are based on the previous study [23, 24], while several changes have been made. The model inputs and the training outputs for the LKE transition model and the $k-\omega$ turbulence model are introduced here.

Two terms in the LKE transport equations are trained. Their common inputs are a new and more concise set of input variables, compared to that previously used [23, 24], developed based on the Buckingham Π theorem [26], shown in Table 1. All P_i (where i=1, 2,...6) are sensitive to transition. In addition, random constants C_m and mathematical operators including plus $(+)$, minus $(-)$ and multiply $(\times)$ are provided as inputs to the GEP algorithm to generate the LKE model corrections. Other mathematical operators such as the exponential, logarithm, and tangent can

Table 1. Flow feature inputs in transition model and their physical interpretation

Transition inputs	Expressions	Physical interpretation
P_1	$\frac{k_l}{\nu\Omega}$	Similar to P_5, but based on k_l
P_2	$\frac{\Omega y}{U}$	The ratio of wall distance to a length scale representative of separated laminar flow [1]
P_3	$\frac{y}{l_t}$	The ratio of wall-distance to turbulent length scale
P_4	$\frac{\sqrt{k}y}{\nu}$	Wall-distance Reynolds number
P_5	$\frac{k}{\nu\Omega}$	The time scale ratio of molecular diffusion to small-scale turbulence (a bypass transition marker).
P_6	$\frac{\sqrt{k}}{\Omega y}$	The ratio between slow and rapid pressure fluctuations (a bypass transition marker).

also be included during the training. However, these operators are not included in this study to keep the trained expressions as simple as possible.

The first training output adjusts the LKE production, replacing the baseline formulation in Eq. (3). It is the $f_1(P_i)$ in the laminar eddy-viscosity ν_l with the input P_i from Table 1:

$$\nu_l = f_1(P_i) y \sqrt{k_l}\,. \tag{5}$$

where y is wall distance. Note that all the inputs are not scaled so that their original magnitude information can be kept during the training. To achieve realizability of the LKE production term, a limiter $\max(f_1(P_i), 0)$ is used to ensure $f_1(P_i) > 0$. Another limiter $\min(f_1(P_i), 0.01\frac{\Omega y}{U})$ (U is the mean velocity, 0.01 is used for the LS89 baseline) is employed to avoid numerical instabilities possibly caused by unreasonably large LKE production.

The second training output $f_2(P_i)$ controls the energy transfer from LKE to TKE. This transfer process starts when $f_2(P_i)$ is larger than 0:

$$\psi = \max(f_2(P_i), 0)\,, \tag{6}$$

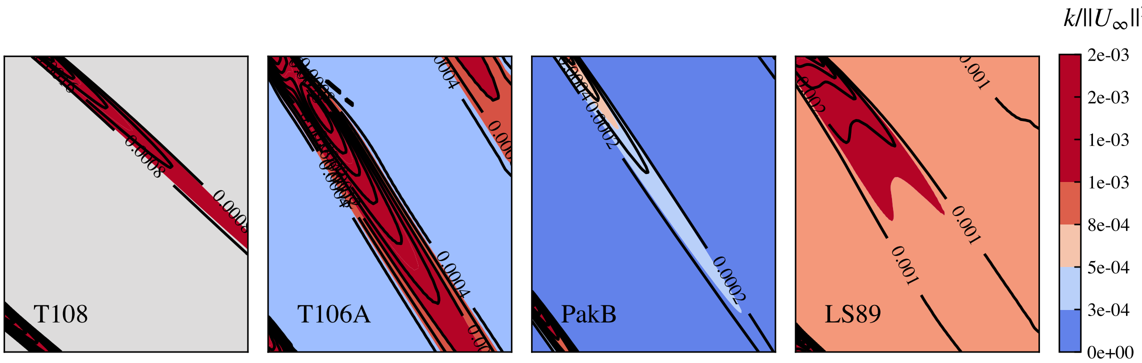

Fig. 2. Training regions of the turbulence model highlighted by TKE

replacing the baseline formulation of ψ in Eq. (4). To summarize, two outputs sharing the same set of inputs, given in Table 1, will be trained to revise the LKE transition model. One is $f_1(P_i)$ ($f_1(P_i)y$ replaces the $C_1\delta_\Omega$ in the baseline) to adjust the LKE production magnitude, and the other is $f_2(P_i)$ ($f_2(P_i)$ replaces $R_y - C_4$) which determines where to activate the energy transfer from LKE to TKE.

Apart from the transition model, the turbulence model is also revised to further improve the wake loss prediction. The training of both models is kept spatially separated. Near the wall, only the LKE transition model is trained. As the LKE transfer term is used to balance the energy both in the transition and turbulence model, it will inevitably change the transfer term in the turbulence model near the wall. Other than this, no change is made to the turbulence model in this region. In the wake region, only the turbulence model is revised. As shown in Fig.2, the training region is limited with two conditions. The first activates training at a certain distance away from the trailing edge [27]. The second is delineating the wake region by a preset threshold value of TKE.

A nonlinear correction is trained to supplement the Boussinesq approximation in the baseline turbulence model. The basic approximation assumes the Reynolds stress $\boldsymbol{\tau}_{ij}$ is proportional to the deviatoric part of the mean strain rate $\boldsymbol{S}^*_{ij}$. As shown in Eq.(7), the Reynolds stress can be divided into isotropic and anisotropic stresses. Based on Pope's theory [28], the correction, an extra anisotropic stress multiplied with $2\rho k$ is added as:

$$\boldsymbol{\tau}_{ij} = \underbrace{\frac{2}{3}\rho k \boldsymbol{\delta_{ij}}}_{\text{isotropic}} - \underbrace{2\mu_T \boldsymbol{S}^*_{ij}}_{\text{anisotropy}} + \underbrace{2\rho k \boldsymbol{a}_{ij}}_{\text{extra anisotropy}} \quad . \tag{7}$$

For statistically two-dimensional flows, $\boldsymbol{a}_{ij}$ consists of three independent tensor bases ($\boldsymbol{V}^1_{ij}, \boldsymbol{V}^2_{ij}$ and $\boldsymbol{V}^3_{ij}$) and two non-zero independent invariants I_1, I_2 [28, 29]:

$$\boldsymbol{a}_{ij} = g_1(I_1, I_2)\boldsymbol{V}^1_{ij} + g_2(I_1, I_2)\boldsymbol{V}^2_{ij} + g_3(I_1, I_2)\boldsymbol{V}^3_{ij}, \tag{8}$$

with $\boldsymbol{V}^1_{ij} = \boldsymbol{s}_{ij}$, $\boldsymbol{V}^2_{ij} = \boldsymbol{s}_{ik}\boldsymbol{w}_{kj} - \boldsymbol{w}_{ik}\boldsymbol{s}_{kj}$ and $\boldsymbol{V}^3_{ij} = \boldsymbol{s}_{ik}\boldsymbol{s}_{kj} - \frac{1}{3}\boldsymbol{\delta}_{ij}\boldsymbol{s}_{mn}\boldsymbol{s}_{nm}$. Here, $\boldsymbol{s}_{ij}$ and $\boldsymbol{w}_{ij}$ are non-dimensionalized strain and rotation rate tensors, respectively, given by $\boldsymbol{s}_{ij} = 1/\omega \boldsymbol{S}^{'}_{ij}$ and $\boldsymbol{w}_{ij} = 1/\omega \boldsymbol{\Omega}_{ij}$. Note that the third tensor used in this paper is from [29] rather the one in [28]. Either of them can be chosen because they are directly proportional to each other.

In addition to the same set of constants and mathematical operators as in the transition model corrections, the inputs for the $k-\omega$ turbulence model corrections are:

$$I_1 = \boldsymbol{s}_{mn}\boldsymbol{s}_{nm}; I_2 = \boldsymbol{w}_{mn}\boldsymbol{w}_{nm}. \tag{9}$$

The model outputs, g_1, g_2 and g_3 in Eq. (8), adjust the nonlinear extra anisotropy stress and thus change the turbulence diffusion.

The CFD-Driven training framework

As shown in Fig. 1, the current multi-case multi-objective CFD-Driven training framework consists of two parts, *i.e.* the ML algorithm and the CFD calculations, which are closely coupled in the training process. For the ML algorithm, GEP is used to generate the corrections for the LKE transition and $k-\omega$ turbulence models with given inputs, as discussed above. GEP is chosen as it produces models in symbolic form, which as will be demonstrated later helps the interpretation of the models and allows for further manipulation. The trained expressions are then inserted into CFD solvers, and then tested in realistic CFD calculations in every training iteration. Including CFD-feedback in model training has previously been shown to substantially increase the usability of the obtained models [30]. One of the key novelties of the current study is that instead of training models only on data of one case, CFD of multiple turbine cases are simultaneously run for each candidate model in order to increase generalizability of the resulting model.

Table 2. Parameters for the training and testing turbine cases

Train/Test	Types	Cases	Re_{is}	Ma_{is}	Flow features	Grid points in O-H Mesh
Train	LPT	T106A	$100k$	0.4	closed separation	$641 \times 101 + 71 \times 121$
Train	LPT	T108	$100k$	0.6	separation	$661 \times 101 + 121 \times 141$
Train	HPT	LS89	$1,000k$	0.92	bypass transition and shocks	$1061 \times 73 + 81 \times 321$
Test	LPT	PakB	$100k$	0.9	separation	$561 \times 65 + 145 \times 121$
Test	LPT	T108	$120k$	0.6	separation	$661 \times 101 + 121 \times 141$

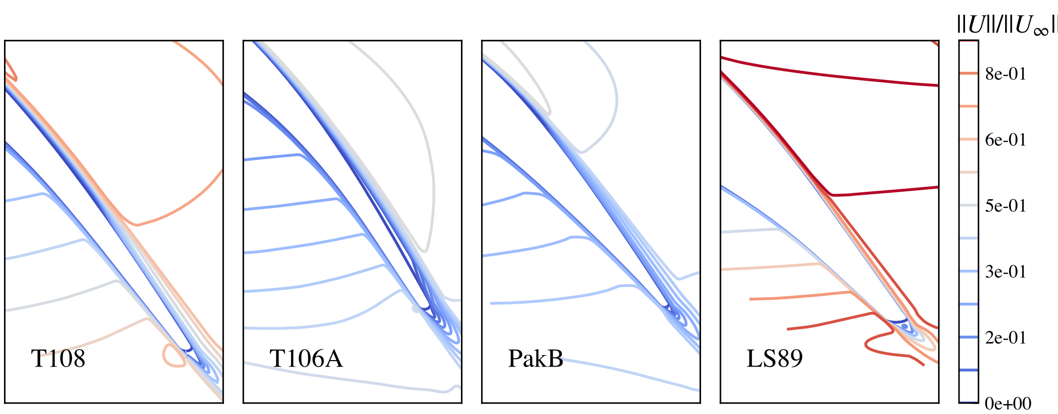

Fig. 3. The velocity magnitude of different turbine cases near their trailing edge

The construction of the cost function is also critical to the data-driven training process as it directs GEP to train models toward the desired outcome. In the present study, the model performance is evaluated based on multiple objectives. To be specific, cost functions are defined here for different quantities of interest, considering the pressure coefficient C_p, the wall shear stress τ_w, and the kinetic wake loss (Ω^*) at certain locations, as

$$
\begin{aligned}
J^{C_p} &= \frac{1}{L_x}\sum_{i=1}^{n}\left(\frac{C_p^{\text{truth}}(x_i) - C_p^{\text{(U)RANS}}(x_i)}{\max_x(C_p^{\text{truth}})}\right)^2,\\
J^{\tau_w} &= \frac{1}{L_x}\sum_{i=1}^{n}\left(\frac{\tau_w^{\text{truth}}(x_i) - \tau_w^{\text{(U)RANS}}(x_i)}{\max_y(\tau_w^{\text{truth}})}\right)^2,\\
J^{\Omega} &= \frac{1}{L_y}\sum_{i=1}^{n}\left(\frac{\Omega^{*\text{truth}}(y_i) - \Omega^{*\text{(U)RANS}}(y_i)}{\max_y(\Omega^{*\text{truth}})}\right)^2.
\end{aligned}
\tag{10}
$$

L_x represents the location along the axial chord and L_y is along the pitchwise direction.

Note that the components of the cost function from different turbine cases are then divided by their baseline errors (see in Eq. (11)) before summing them up to to avoid specific errors dominating the optimization. By summing up the same variable of interest over different cases, the trained models are expected to improve predictions for cases with different physics. Furthermore, instead of simply summing up the different cost functions J^{MOi}, the multi-objective algorithm that exploits a Pareto ranking approach is used to evaluate the model performance [25].

$$
\begin{aligned}
J^{MO1} = \sum_{j=1}^{3}\left(\frac{J_j^{C_p}}{J_{Baseline,j}^{C_p}}\right), J^{MO2} &= \sum_{j=1}^{3}\left(\frac{J_j^{\tau_w}}{J_{Baseline,j}^{\tau_w}}\right),\\
J^{MO3} &= \sum_{j=1}^{3}\left(\frac{J_j^{\Omega^*}}{J_{Baseline,j}^{\Omega^*}}\right).
\end{aligned}
\tag{11}
$$

It should be emphasized that another strength of the CFD-Driven approach is that it does not require full spatial data sets which are usually hard to obtain from experiments. In the current study for every turbine case only limited truth data in the form of one-dimensional profiles is utilized. These include C_p or Ma_{is}, τ_w on the suction side near the trailing edge or Ω^* profiles in the wake region. More detailed information about the ML framework can be found in [30, 25].

CFD settings

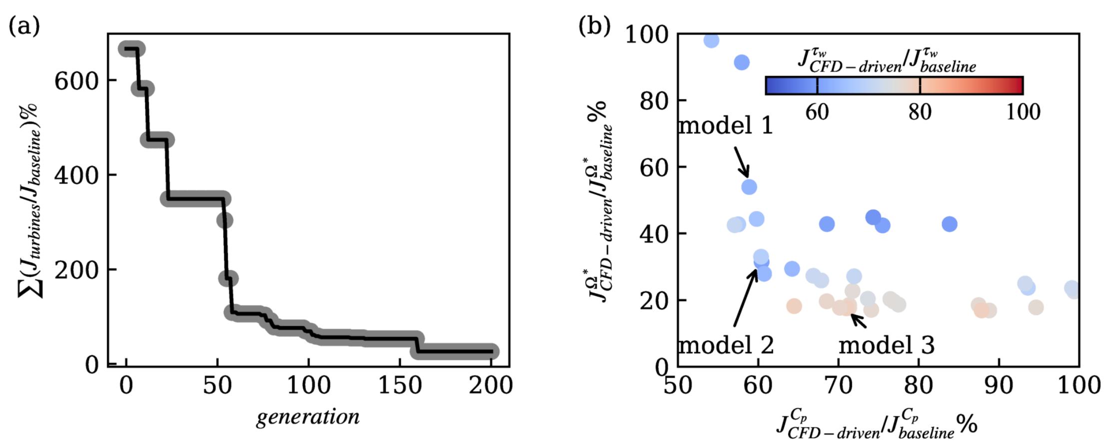

Fig. 4. Model evaluation: (a) the evaluation of averaged cost function value along training generation; (b) Pareto analysis on errors of the blade surface and wake parameters

As shown in Table 2, two LPT (T106A and T108) and one HPT (LS89) configurations are used as the training cases, while another LPT profile (PakB) and a T108 at a higher Reynolds number are selected as the testing cases. The cases are selected to incorporate as many transition phenomena as possible. To visualize the transition, Fig.3 shows contour plots of the velocity magnitude for each case. As described in Table 2, a close separation bubble on the T106A suction side is observed. For T108 and PakB, open separation is observed near the trailing edge. LS89 undergoes bypass transition.

The CFD solver used in this study is called TRAF [31]. Because the present calculations focus on the blades' midspan sections, two-dimensional plane-cut calculations can be run to save computational costs [2]. Steady and compressible RANS are conducted for the LPT cases, while URANS is applied for the HPT (LS89) to capture the strong vortex shedding. Table 2 summarizes the mesh and inflow information of all the turbine cases conducted in this study. A dual-time-stepping method and a 2nd order cell-centered spatial scheme are employed. In terms of the boundary condition of LKE, the inlet condition for k_l is: $k_{l,\infty} = k_\infty = 3/2 Tu_\infty^2 U_\infty^2$. The wall boundary condition is set with $k_l = 0$. More details for the (U)RANS calculations can be found in [32] for T106A, [33] for T108, and [27] for PakB.

The ground truth data for model training are obtained either from high-fidelity simulations or experiments, specifically direct numerical simulation (DNS) for T106A [2], experiments for T108 [34, 33] and PakB [35], and large eddy simulation (LES) for LS89 [36].

RESULTS & DISCUSSION

This section details how the ML-trained models are selected, and their performance on the training turbine cases is presented. The common characteristics of selected trained models are summarized and analyzed. The last part shows the numerical prediction from the trained model on two cases different from the training cases: the testing cases PakB and T108 at $Re_{is} = 120k$.

Model selection and performance

Fig.4 (a) tracks the minimum average value of all the cost function components over every training generation. It indicates that the training process seems converged after roughly 160 generations. Fig.4 (b) shows the distribution of three cost function components (C_p, τ_w (shown in colour) and Ω^*, see Eq. (10)) from the trained models at the last training generation. To facilitate the model selection, these values are divided by the baseline errors and then presented in percentage form. Hereafter, we select models that have small errors for either pressure coefficient or isentropic Mach number, wake loss and wall shear stress as highlighted in Fig.4 (b). Three models are selected. Model 1 has low J^{C_p}. Model 2 has low J^{C_p}, J^{τ_w} and J^{Ω^*}. Model 3 has low J^{Ω^*}. In this paper, they are denoted as the 'CFD-Driven model 1/2/3'.

We turn our attention first to the comparison of the pressure coefficient or isentropic Mach number from the ground truth, baseline model, and CFD-Driven models, as shown in Fig.5 (a)-(c). In general, improvements are obtained with the trained models 1/2/3, especially in the transition region for the LPTs (T108 and T106A), mostly visible in the zoom-in view. The baseline LKE model (in blue) shows a larger slope of pressure coefficient or isentropic Mach number close to the trailing edge than the ground truth data. This means that the baseline LKE model tends to overpredict the pressure or velocity gradient in the adverse pressure region, no matter whether

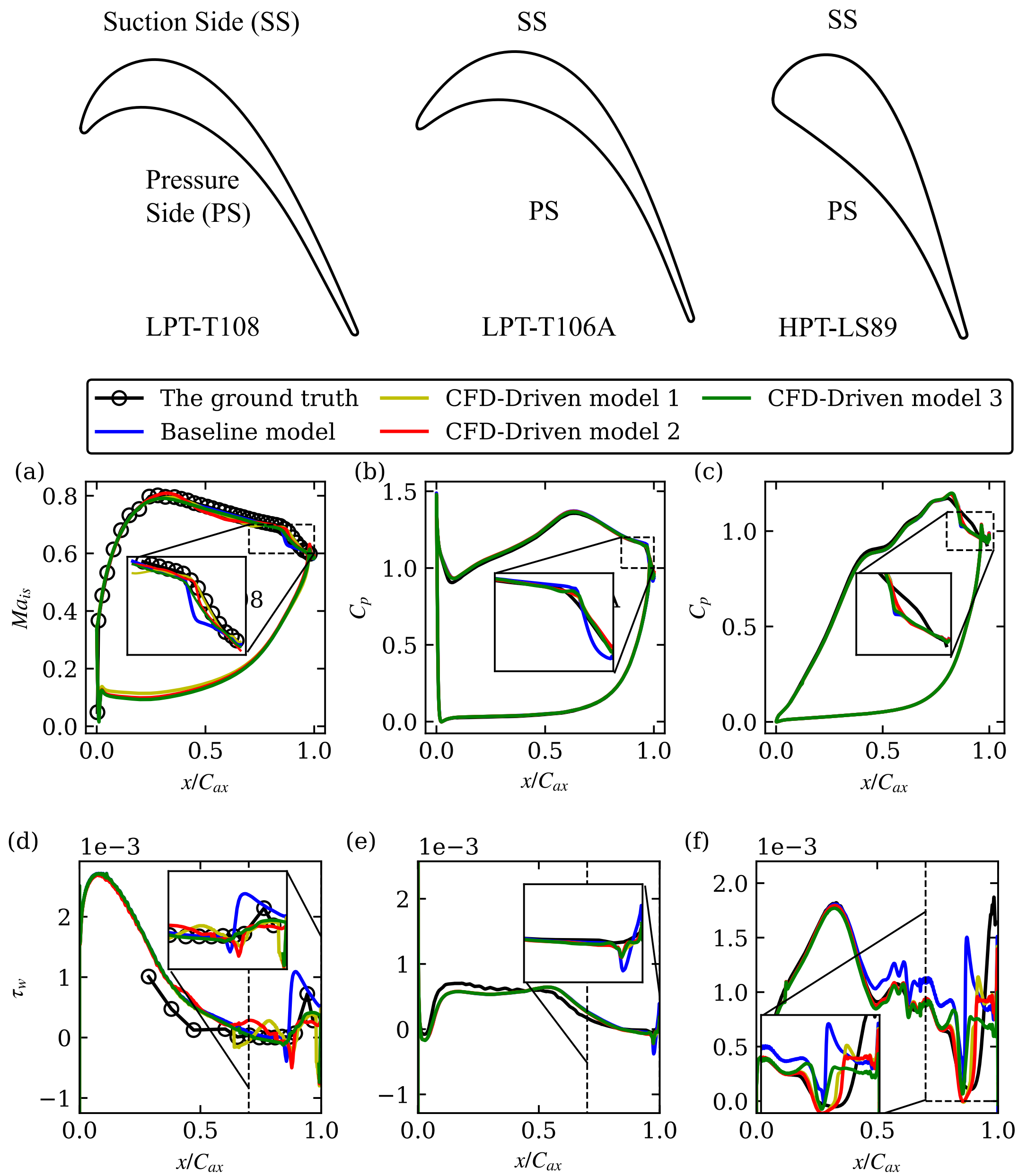

Fig. 5. The comparison of the pressure coefficient or mach number and wall shear stress between the ground truth, baseline, and CFD-Driven models

separation-induced or bypass transition occurs. Nonphysical phenomena may be predicted as a result of these large gradients such as the presence of a nonphysical shock for the LS89 case. On the other hand, the CFD-Driven models have better agreement with the reference data and are able to improve the prediction of the gradients in the transition region.

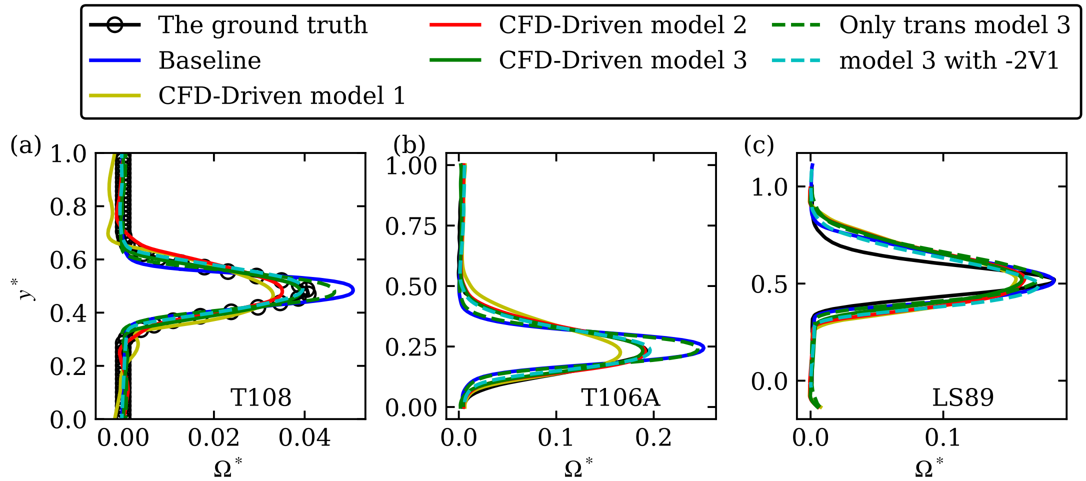

Fig. 6. Comparison of the wake loss profiles: (a) T108 at $x/C_{ax} = 1.55$; (b) T106A at $x/C_{ax} = 1.29$; (c) LS89 at $x/C_{ax} = 1.25$

To further illustrate the transition phenomena, the wall shear stress on the suction side, and a zoom-in view, from the ground truth data, baseline and the CFD-Driven models are plotted in Fig.5(d)-(f). Similar to the pressure coefficient or isentropic Mach number shown in Fig.5(a)-(c), the major differences can be observed near the trailing edge. For the T108 case shown in Fig.5(d), no negative wall shear stress is observed in the experimental data while negative values are indeed found from the baseline calculation. However, there is possibly some uncertainty in the experimental data, because the hot-films used to measure wall shear stress may be too thick to be fully immersed in the boundary layer. By improving the prediction of the maximum location of τ_w near the trailing edge and its gradient, all CFD-Driven models give better Ma_{is} prediction as shown in Fig.5(a). Note that the wall shear stress predicted by model 3 is much smoother than when using models 1 and 2, indicating that model 3 is the most numerically stable. For the T106A case shown in Fig.5(e), two closed separation bubbles can be identified, one near the leading edge and one near the trailing edge. For the latter separation bubble, the baseline model predicts a larger extent than the high-fidelity result while all CFD-Driven models 1, 2 and 3 provide a closer prediction to the high-fidelity results. Fig.5(f) shows the wall shear stress distribution for the LS89 case. The location where the wall shear stress suddenly increases identifies the bypass transition onset. It turns out all the CFD-Driven models perform better than the baseline upstream of the

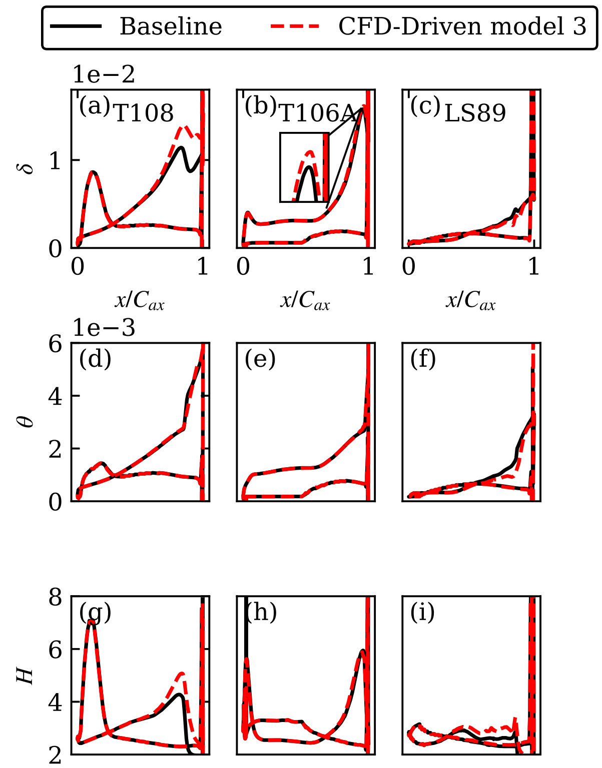

Fig. 7. Comparison of the boundary layer thickness, momentum thickness and shape factor between baseline and CFD-Driven model 3

bypass transition onset. Both CFD-Driven models 1 and 2 show a more accurate prediction of the transition onset while CFD-Driven model 3 gives an earlier onset prediction similar to the baseline. We remark that the wall shear stress calculated by all CFD-Driven models does not reach the same amplitude as the ground truth data. After the transition, the LKE decreases and TKE grows where the τ_w is then mainly decided by TKE. However, no turbulence correction is made in this near-wall region to further increase TKE, which will be considered for future work.

In addition to the on-blade flow behaviour, the kinetic wake-loss is also a parameter of primary interest and is presented in Fig.6. For the LPT cases T108 and T106A, shown in Fig.6(a) and (b), the baseline predictions display narrower and bigger peak wake loss values than the ground truth data. All the CFD-Driven models, on the other hand, are able to correct this behavior and produce predictions closer to the ground truth. For the HPT LS89 case shown in Fig.6(c), the prediction of the wake width is not much changed compared to the baseline and actually a little worse at the wake peak. However, it should be noted that the baseline prediction already is rather good, owing to the unsteady RANS resolving the vortex shedding. We believe this small deterioration in prediction is acceptable given the significant improvement of the same models for the LPT cases. This shows that a single set of models, developed on multiple training cases, is able to significantly improve predictive performance for the cases where the baseline models performed badly, while a similar prediction to the baseline is obtained for cases in which the baseline already performs quite well, i.e. here the URANS of the HPT LS89 case.

In order to differentiate whether the changes to the wake prediction come from the trained transition or turbulence models, the wake loss obtained by running a test using only the updated transition model of the CFD-Driven model 3, but the baseline turbulence model, is also presented and compared with the full set of CFD-Driven model 3. As shown by the dashed green lines in Fig.6, the revised transition model can provide a better prediction of wake loss but not as good as when also including the trained turbulence model. Hence, training the transition model alone can not provide satisfactory results for wake loss. We believe the improved flow coming off the blade by the trained transition model and the higher levels of turbulent diffusion predicted by the trained turbulence model are both required to improve the prediction of the wake loss.

We also compare the boundary layer thickness, momentum thickness and shape factor on the suction side from CFD-Driven model 3 with the predictions from the baseline, as shown in Fig.7. Since the boundary layer thickness in the transition regions for the LPTs (T108 and T106A) predicted by CFD-Driven model 3 is thicker than when using the baseline, this contributes to the widening of the wake width and the improvement can be noticed in Fig.6 (a) and (b). In contrast to the LPT cases, the width of the wake loss profile of the HPT LS89 shown in Fig.6 is too wide. That is why the CFD-Driven model 3 tries to decrease the boundary thickness in Fig.8 (g) and (i). In terms of shape factor, the larger shape factors given by CFD-Driven model 3 over the baseline indicate smaller momentum thickness and thus reduce the wall shear stress in Fig.5 (d) and (f). For the T106A case, the difference is too small to be observed.

We also conducted single-case training for each training turbine case, with the results shown in the Appendix. The purpose of these additional training runs was to find a reference 'best

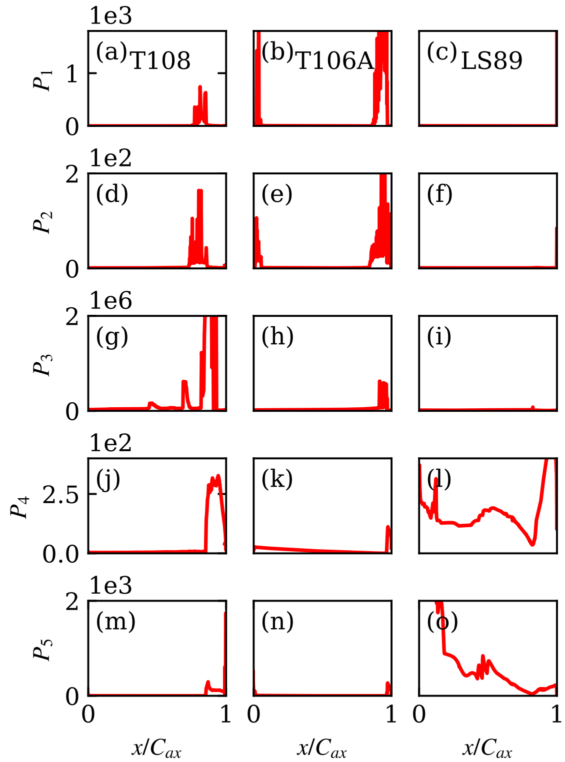

Fig. 8. The distribution of P_1, P_2, P_3, P_4 and P_5 on the suction side for T108, T106A and LS89

model', essentially an entitlement, against which we could evaluate the multi-case trained model performance. Note that the CFD-Driven model 3 shows similar performance to every single-case trained model for each case. This promising result means one model performs well across different transition paths without the need for manually changing the coefficients in the LKE model.

Model analysis

In order to understand why the trained models perform better than the baseline model, the ML-trained explicit expressions are now analyzed, and the transition inputs P_i and the LKE transport components such as the LKE production and transfer terms will be extracted in this subsection.

The following are the expressions in the LKE transition model given by GEP. The trained terms in the LKE production and transfer of CFD-Driven model 1 are:

$$
\begin{aligned}
f_1^{model1}(P_i) &= (1.2P_1 - 1.09)(P_2 - 2.91), \\
f_2^{model1}(P_i) &= -P_1 - P_2 - P_3 + P_5 - P_6 - 0.7.
\end{aligned}
\tag{12}
$$

The trained terms of CFD-Driven model 2 are:

$$
\begin{aligned}
f_1^{model2}(P_i) &= (1.2P_1 - 1.09)(P_2 - 2.91) \\
f_2^{model2}(P_i) &= -2P_1 - 2P_3 + P_5 - 0.18.
\end{aligned}
\tag{13}
$$

The CFD-Driven transition model 3 is:

$$
\begin{aligned}
f_1^{model3}(P_i) &= -0.09P_4(P_2 - 2.15)(P_1P_4 - P_2 - 2P_3 + 0.91) \\
f_2^{model3}(P_i) &= -P_1 - P_2 - P_3 + P_5 - P_6 - 0.7.
\end{aligned}
\tag{14}
$$

We start by observing the common characteristics of GEP-trained models in the LKE production and transfer terms. The physical representation of P_i is given in Table 1. For the LKE production term, we notice that both P_1 and P_2 commonly occur. The appearance of P_1 means the k_l is closely related to LKE production. P_2 on the other hand brings the free stream velocity information to LKE prediction. These observations are consistent with the original construction of the LKE production term, in which the laminar eddy viscosity is $\nu_l = C_1\sqrt{k_l}\delta_\Omega$ in Eq.(3) and the estimator of shear-layer vorticity thickness is $\delta_\Omega = \min\left(\frac{\Omega y^2}{U}, 2\right)$.

For the transfer term, the combination of negative P_1 and P_3 and positive P_5 is present in all the three CFD-Driven models. If we merge P_1 and P_5 as:

$$
f_2 = -P_1 - P_3 + P_5 = (P_5 - P_1) - P_3 = \underbrace{\frac{k - k_l}{\nu\Omega}}_{\text{transition sensor}} - \underbrace{\frac{y}{l_t}}_{\text{threshold}},
\tag{15}
$$

we find that this expression follows a similar construction pattern as the one in the baseline LKE transfer term, see Eq.(4). This leads to an activation of the energy transfer when the transition sensor reaches the threshold. Here, the transition sensor represents a non-dimensional variable related to transition phenomena. The sensor given by the CFD-Driven models is $\frac{k-k_l}{\nu\Omega}$, while for the baseline LKE model (see Eq.4) it is based on the wall distance Reynolds number P_4. As for the threshold, the CFD-Driven model gives a variable that is the ratio of wall-distance to turbulent length scale $\frac{y}{l_t}$, while the baseline uses a constant (see Eq.4). In terms of the selection of transition sensor, both P_4 and P_5 are identified as important quantities for the shear-sheltering in attached boundary layer states [15, 17, 37, 38]. Shear-sheltering is a physical phenomenon that damps the small-scale free-stream fluctuations penetrating the pre-transitional boundary layer, confirmed by [39, 40, 41]. Walters and Cokljat [17] defined a shear-sheltering factor based on the ratio of the diffusive and convective time scales P_5. Assuming the wall-normal fluctuation length scale in the laminar portion of a pre-transitional boundary layer, $\sqrt{k}$ is replaced by $y\Omega$ and thus P_4 is used in the definition of the shear factor in [15, 38]. To summarize, the obtained CFD-Driven model suggests replacing P_4, as used in the baseline, with P_5 as the transition sensor, and a non-constant parameter as the threshold.

Fig.8 plots the distribution of P_i within the boundary layer on the suction side for every training turbine case. For the T108 case, shown in the first column of Fig.8, we notice that all flow features P_i are quite large near the open separation region. For the T106A case, the second column, P_i takes the largest values in the separation bubble, identified by the wall shear stress distribution in Fig.5. This observation suggests that P_i are quite sensitive to the separation-induced transition. For the LS89 case presented in the third column, P_4 and P_5 vary more than P_1, P_2, and P_3. This is related to the shear-sheltering effect and explains why P_4 and P_5 are often used for activation of bypass transition in transition models [6].

We then shift our focus to analyze the LKE production, transfer terms, LKE, and TKE on the suction sides for all the training cases. We also plot these variables from the single-case trained models (their performance can be found in the Appendix) to confirm the respective correction trends. The expressions and model performance from single-case training can be found in the

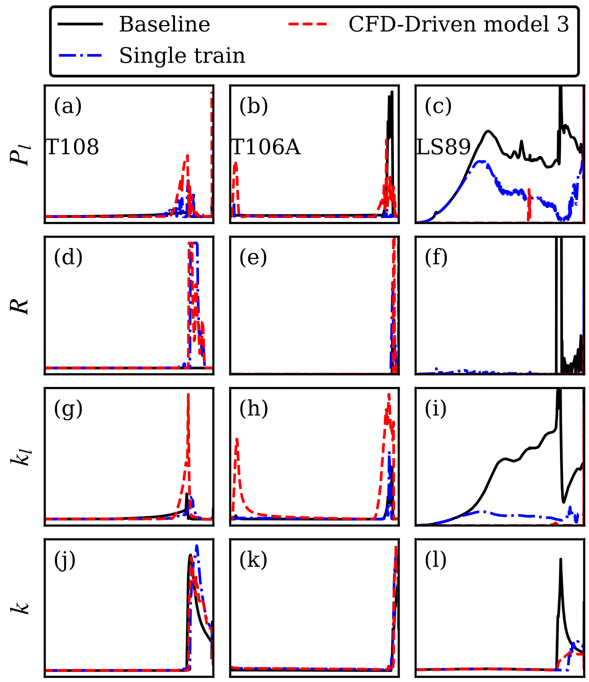

Fig. 9. Comparison of the baseline, single-case trained and multi-case trained models on LKE production, transfer terms, LKE and TKE

Appendix. The comparison of these physical terms is given in Fig.9 (using CFD-Driven model 3 as an example). The first column in Fig.9 shows the LKE-related quantities and TKE for the T108 case. Before the transition onset, all the models give nearly zero LKE production, transfer, and thus LKE and TKE. This common prediction is physical due to the existence of the laminar region. As shown in Fig.9(g), after the transition onset, both single- and multi-case trained models decrease LKE gradually instead of immediately back to zero as the baseline. This agrees with the statement in [15] that a small amount of LKE still exists in the viscous layer after transition.

The second column in Fig.9 presents the same quantities for the T106A. As shown in Fig.5(e), there are two separation bubbles on the suction side. The LKE production P_l and k_l are quite large near both bubbles, while the LKE transfer term R and k only show strong variation close to the one near the trailing edge. This makes sense due to R and k representing the turbulent state. The large values near the bubble also explain why the trained models easily improve the C_p and τ_w near the trailing edge and not across the whole suction side as seen in Fig.5(e). In other words, the transition inputs are more sensitive to the separation bubble, which is consistent with

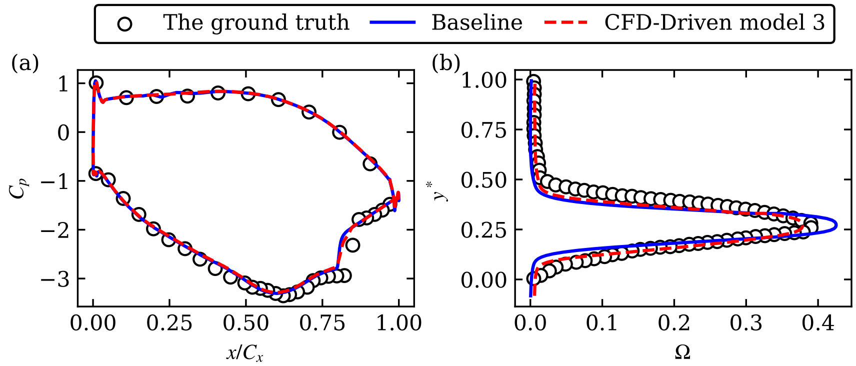

Fig. 10. The pressure coefficient and wake loss of PakB with the CFD-Driven model

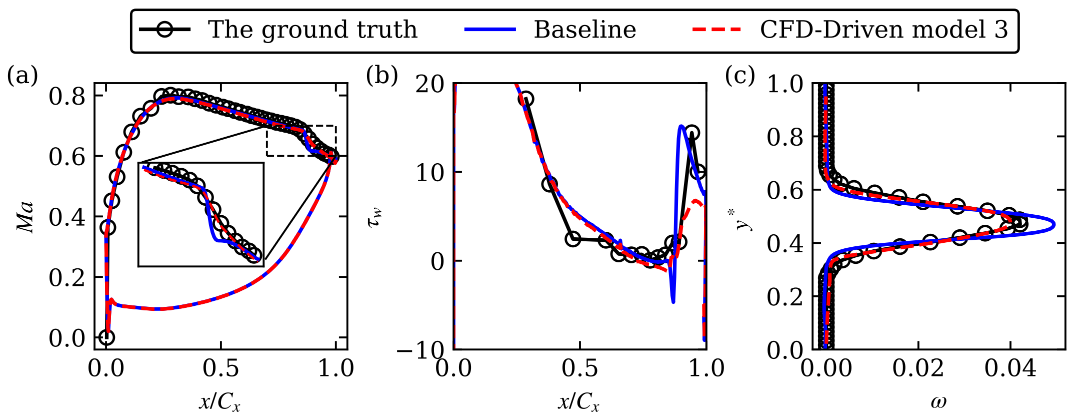

Fig. 11. The pressure coefficient and wake loss of T108 $Re_{is} = 120k$ with the CFD-Driven model

the analysis of Fig.8.

The last column in Fig.9 plots the same quantities for the LS89 case. Both single- and multi-case trained models produce less LKE than the baseline to obtain smaller τ_w in Fig.5. However, the insufficient LKE and less transfer to TKE in the bypass transition region also lead to values of τ_w that are too small near the trailing edge, as seen in Fig.5 (f).

It is worth emphasizing that the trained models produce larger LKE than the baseline for LPTs while the opposite is true for the HPT case. This means the same trained models are able to provide different correction trends for different transition modes.

Finally, we also investigate the turbulence model correction. The extra anisotropy stress given by CFD-Driven model 1 is:

$$\begin{aligned}\boldsymbol{a}_{ij}^{model1} =& (-I_1^2 - 2.43I_1 - 3.1)\boldsymbol{V}_{ij}^1 + (2I_1^2 - 2I_2 + 2.38)\boldsymbol{V}_{ij}^2 + \\ & (0.24(I_2+1)(-1.8I_1 + 1.8I_2 + 0.36))\boldsymbol{V}_{ij}^3.\end{aligned} \tag{16}$$

The trained expression in CFD-Driven model 2 is:

$$\begin{aligned}\boldsymbol{a}_{ij}^{model2} =& (-I_1^2 - 3I_1 - 2)\boldsymbol{V}_{ij}^1 + (-I_1(I_2 + 0.15) + 5.42)\boldsymbol{V}_{ij}^2 + \\ & (0.43I_2(I_2+0.2)(I_2+1)(I1 - I2 + 0.1))\boldsymbol{V}_{ij}^3.\end{aligned} \tag{17}$$

For the CFD-Driven model 3:

$$\begin{aligned}\boldsymbol{a}_{ij}^{model3} =& (-I_1^2 - 3I_1 - 2)\boldsymbol{V}_{ij}^1 + (-I_1I_2 + 3I_1 + 2)\boldsymbol{V}_{ij}^2 + \\ & (-I_2(I_2+1.0) - 1.8)\boldsymbol{V}_{ij}^3.\end{aligned} \tag{18}$$

Similar analysis of the turbulence model as in [42] can be performed. Here we take CFD-Driven model 3 as an example. Keeping only the leading term in Eq.(16) and considering that the magnitudes of I_1 and I_2 are quite small, the trained extra anisotropic stress can be simplified as $\boldsymbol{a}_{ij} = (-2)\boldsymbol{V}_{ij}^1$. With $\mu_t \boldsymbol{S}_{ij}^{'} = \rho k \boldsymbol{V}_{ij}^1$ and Eq.(16), we obtain:

$$\boldsymbol{\tau}_{ij}^{CFD-Driven} = \frac{2}{3}\rho k \boldsymbol{\delta}_{ij} - 2\mu_t(1.0+2)\boldsymbol{S}_{ij}^{'}. \tag{19}$$

The above correction of increasing turbulence diffusion is found to be consistent with the single-case trained model of [24], where the coefficient also equals roughly 2. Hence, both training approaches indicate that the baseline approximation cannot provide enough turbulence diffusion for 2D turbine wake predictions. More diffusion is needed to decrease the amplitude of the wake peak and increase the wake width. The fact that the revised turbulence models still look very similar to the Boussinesq approximation with only an increase in the coefficient of anisotropic stress is promising. This small change brings improved results for 2D RANS calculations of turbine cases and maintains a similar computation cost. This is also further validated by testing the performance of the transition model from CFD-Driven model 3 and only the term $-2\boldsymbol{V}_{ij}^{1}$ of the anisotropic stress correction for the turbulence model, shown with the dashed blue line in Fig. 6. This result agrees well with the full CFD-Driven model 3.

Cross validation

We select the CFD-Driven model 3 to conduct the cross-validation on two testing cases. One is the T108 profile at a higher Reynolds number ($Re_{is} = 120k$) than the one used as the training case and the other is a different geometry, the PakB section at $Re_{is} = 100k$. CFD-Driven model 3 is used to perform RANS calculations of the two testing cases, with the results shown in Figs.10 and 11. Overall, the numerical predictions from the baseline and the CFD-Driven model 3 give stable predictions and both agree quite well with the reference data. For the on-blade parameters in Fig.10 (a) and in Fig.11 (a), the CFD-Driven model 3 performs better in the transition region by decreasing the gradient of Ma_{is} or C_p. In the wake region, the CFD-Driven model 3 predicts wider wake loss and smaller wake peak that agrees better with the ground truth in Fig.10 (b) and 11 (c). In Fig.11(b), it can be noticed that the prediction of wall shear stress τ_w for the T108 case gives a smaller amplitude than the experiment and baseline, even though it improves the calculation of the amplitude location near the trailing edge.

CONCLUSIONS

In this study, we presented an approach to develop a more general LKE transition model that can capture the most common transition phenomenon in gas turbines. They are the separation-induced transition that is often found in LPTs and bypass transition mostly occurring in HPTs. To achieve this, the original single-case CFD-Driven framework used in [24] was extended to a multi-case training approach. Several LPT and HPT configurations, including T108, T106A, and LS89 were used for model training in the present framework. Unsteady RANS was employed for the

LS89 case to capture the strong vortex shedding near the trailing edge, constituting the first use of URANS feedback in data-driven model training. Moreover, more concise inputs to the transition model were proposed and utilized in this study. The following conclusions have been obtained:

1. By training the LKE production and transfer terms with the six input features, multi-case CFD-Driven transition models are obtained by GEP that perform as well on all cases as single-case trained models developed for each case individually. This means that there is no need for a user to specify different coefficients to predict different transition modes. Instead the trained models, by using the appropriate flow-dependent input features, can automatically adapt to the different transition scenarios.
2. Opposite correction trends for the separation-induced and bypass transition cases are found to be required by extracting and analyzing the trained LKE production, transfer terms, LKE and TKE. The CFD-Driven models produce and transfer more LKE close to the trailing edges of LPTs while they produce and transfer less LKE in the HPT case.
3. The training of both transition and turbulence models benefits the wake loss prediction. The trained transition models provide better prediction of the flow coming off the trailing edge and thus improve the wake width. The CFD-Driven turbulence correction provides extra anisotropy stress to further increase the turbulence diffusion. As a result, wider and smaller peak-amplitude wakes are obtained that better approximate the ground truth data.
4. By analyzing the common characteristics of the multi-case trained models, some suggestions are given by the ML algorithm to construct the transition model. For the LKE production term, a time scale ratio containing LKE is suggested to be considered. For the transfer term, a non-constant threshold is recommended to activate the energy transfer.

ACKNOWLEDGEMENTS

Y. Zhao was supported by the National Natural Science Foundation of China (Grant No. 92152102) and the Advanced Jet Propulsion Innovation Center/AEAC (Funding No.HKCX2022-01-010). R. Pacciani and M. Marconcini acknowledge the financial support from ICSC – Italian Research Center on High Performance Computing, Big Data and Quantum Computing, funded by the European Union – NextGenerationEU (CUP B83C22002830001). H. Akolekar acknowledges the seed grant support funding by IIT Jodhpur. R. D. Sandberg acknowledges funding from the Australian Research Council (Grant FT190100072). Y. Fang is grateful for a Melbourne Graduate Scholarship. This work also acknowledges the computing resources provided by The University of Melbourne's Research Computing Services and the Petascale Campus Initiative.

REFERENCES

[1] Sandberg, R. D., and Michelassi, V., 2019, "The current state of high-fidelity simulations for main gas path turbomachinery components and their industrial impact," *Flow Turbul. Combust.,* **102**(4), pp. 797–848.

[2] Michelassi, V., Chen, L.-W., Pichler, R., and Sandberg, R. D., 2015, "Compressible Direct Numerical Simulation of Low-Pressure Turbines—Part II: Effect of Inflow Disturbances," *J. Turbomach.,* **137**(7), p. 071005.

[3] Mayle, R. E., 1991, "The 1991 IGTI Scholar Lecture: The Role of Laminar-Turbulent Transition in Gas Turbine Engines," *J. Turbomach.,* **113**(4), pp. 509–536.

[4] Ferreira, T. S., Arts, T., and Croner, E., 2019, "On the Influence of High Turbulence on the Convective Heat Flux on the High-Pressure Turbine Vane LS89," *Int. J. Turbomach. Propuls.,* **4**(37), pp. 2–19.

[5] Thermann, H., Müller, M., and Niehuis, R., 2001, "Numerical simulation of the boundary layer transition in turbomachinery flows," In Turbo Expo: Power for Land, Sea, and Air, Vol. 78521, American Society of Mechanical Engineers, p. V003T01A088.

[6] Dick, E., and Kubacki, S., 2017, "Transition models for turbomachinery boundary layer flows: a review," *Int. J. Turbomach. Propuls.,* **2**(2), p. 4.

[7] Steelant, J., and Dick, E., 1996, "Modelling of bypass transition with conditioned Navier–Stokes equations coupled to an intermittency transport equation," *Int. J. Numer. Methods Fluids,* **23**(3), pp. 193–220.

[8] Fürst, J., Příhoda, J., and Straka, P., 2013, "Numerical simulation of transitional flows," *Computing,* **95**(1), pp. 163–182.

[9] Kožulović, D., and Lapworth, B. L., 2009, "An Approach for Inclusion of a Nonlocal Transition Model in a Parallel Unstructured Computational Fluid Dynamics Code," *J. Turbomach.,* **131**(3), p. 031008.

[10] Menter, F. R., Langtry, R. B., Likki, S., Suzen, Y., Huang, P., and Völker, S., 2006, "A correlation-based transition model using local variables—part I: Model Formulation," *J. Turbomach.,* **128**(7), pp. 413–422.

[11] Ge, X., Arolla, S., and Durbin, P., 2014, "A bypass transition model based on the intermittency function," *Flow Turbul. Combust.,* **93**(1), pp. 37–61.

[12] Lodefier, K., and Dick, E., 2006, "Modelling of unsteady transition in low-pressure turbine blade flows with two dynamic intermittency equations," *Flow Turbul. Combust.,* **76**(2), pp. 103–132.

[13] Mayle, R., and Schulz, A., 1996, "The path to predicting bypass transition," In Turbo Expo: Power for Land, Sea, and Air, Vol. 78729, American Society of Mechanical Engineers, p. V001T01A065.

[14] Lardeau, S., Li, N., and Leschziner, M. A., 2007, "Large eddy simulation of transitional boundary layers at high free-stream turbulence intensity and implications for RANS modeling," *J. Turbomach.,* **129**(2), pp. 311–317.

[15] Walters, D. K., and Leylek, J. H., 2004, "A new model for boundary layer transition using a single-point rans approach," *J. Turbomach.,* **126**(1), pp. 193–202.

[16] Walters, D. K., and Leylek, J. H., 2005, "Computational fluid dynamics study of wake-induced transition on a compressor-like flat plate," *J. Turbomach.,* **127**(1), pp. 52–63.

[17] Walters, D. K., and Cokljat, D., 2008, "A three-equation eddy-viscosity model for Reynolds-averaged Navier–Stokes simulations of transitional flow," *J. Fluids Eng.,* **130**(12).

[18] Lardeau, S., Leschziner, M., and Li, N., 2004, "Modelling bypass transition with low-reynolds-number nonlinear eddy-viscosity closure," *Flow Turbul. Combust.,* **73**(1), pp. 49–76.

[19] Pacciani, R., Marconcini, M., Fadai-Ghotbi, A., Lardeau, S., and Leschziner, M. A., 2011, "Calculation of high-lift cascades in low pressure turbine conditions using a three-equation model," *J. Turbomach.,* **133**(3), p. 031016.

[20] Duraisamy, K., and Durbin, P., 2014, "Transition modeling using data driven approaches," In Proceedings of the Summer Program, Stanford CTR, p. 427.

[21] Yang, M., and Xiao, Z., 2020, "Improving the k–ω–γ–Ar transition model by the field inversion and machine learning framework," *Phys. Fluids,* **32**(6), p. 064101.

[22] Wu, L., Cui, B., and Xiao, Z., 2022, "Two-equation turbulent viscosity model for simulation of transitional flows: An efficient artificial neural network strategy," *Phys. Fluids,* **34**(10), p. 105112.

[23] Akolekar, H. D., Waschkowski, F., Zhao, Y., Pacciani, R., and Sandberg, R. D., 2021, "Transition modeling for low pressure turbines using computational fluid dynamics driven machine learning," *Energies,* **14**(15), p. 4680.

[24] Akolekar, H. D., Waschkowski, F., Pacciani, R., Zhao, Y., and Sandberg, R. D., 2022, "Multi-Objective Development of Machine-Learnt Closures for Fully Integrated Transition and Wake Mixing Predictions in Low Pressure Turbines," In Turbo Expo: Power for Land, Sea, and Air, Vol. 86113, American Society of Mechanical Engineers, p. V10CT32A013.

[25] Waschkowski, F., Zhao, Y., Sandberg, R., and Klewicki, J., 2022, "Multi-objective cfd-driven development of coupled turbulence closure models," *J. Comput. Phys.,* **452**, p. 110922.

[26] White, F. M., 1979, *Fluid mechanics* Tata McGraw-Hill Education.

[27] Akolekar, H. D., Zhao, Y., Sandberg, R. D., and Pacciani, R., 2021, "Integration of Machine Learning and Computational Fluid Dynamics to Develop Turbulence Models for Improved Low-Pressure Turbine Wake Mixing Prediction," *J. Turbomach.,* **143**(12).

[28] Pope, S. B., 1975, "A more general effective-viscosity hypothesis," *J. Fluid Mech.,* **72**(2), pp. 331–340.

[29] Gatski, T. B., and Speziale, C. G., 1993, "On explicit algebraic stress models for complex turbulent flows," *Journal of fluid Mechanics,* **254**, pp. 59–78.

[30] Zhao, Y., Akolekar, H. D., Weatheritt, J., Michelassi, V., and Sandberg, R. D., 2020, "RANS turbulence model development using CFD-driven machine learning," *J. Comput. Phys.,* **411**, p. 109413.

[31] Arnone, A., Liou, M.-S., and Povinelli, L. A., 1992, "Navier-Stokes solution of transonic cas-

cade flows using nonperiodic C-type grids," *J. Propuls. Power,* **8**(2), pp. 410–417.

[32] Akolekar, H. D., 2019, "Turbulence model development and implementation for low pressure turbines using a machine learning approach," PhD thesis, University of Melbourne.

[33] Pacciani, R., Marconcini, M., Arnone, A., and Bertini, F., 2011, "An assessment of the laminar kinetic energy concept for the prediction of high-lift, low-reynolds number cascade flows," *P. I. Mech. Eng. A-J Pow.,* **225**(7), pp. 995–1003.

[34] Himmel, C., Thomas, R., and Hodson, H., 2009, "Effective passive flow control for ultra-high lift low pressure turbines," In Eighth European Conference on Turbomachinery Fluid Dynamics and Thermodynamics, March 23-27, Gratz, Austria.

[35] Bons, J. P., Sondergaard, R., and Rivir, R. B., 2001, "Turbine separation control using pulsed vortex generator jets," *J. Turbomach.,* **123**(2), pp. 198–206.

[36] Pichler, R., Sandberg, R. D., Laskowski, G., and Michelassi, V., 2017, "High-fidelity simulations of a linear hpt vane cascade subject to varying inlet turbulence," In Turbo Expo: Power for Land, Sea, and Air, Vol. 50787, American Society of Mechanical Engineers, p. V02AT40A001.

[37] Walters, D., 2009, "Physical interpretation of transition-sensitive rans models employing the laminar kinetic energy concept," *ERCOFTAC Bulletin,* **80**, pp. 67–71.

[38] Kubacki, S., and Dick, E., 2016, "An algebraic intermittency model for bypass, separation-induced and wake-induced transition," *International Journal of Heat and Fluid Flow,* **62**, pp. 344–361.

[39] Jacobs, R. G., and Durbin, P. A., 1998, "Shear sheltering and the continuous spectrum of the orr–sommerfeld equation," *Physics of Fluids,* **10**(8), pp. 2006–2011.

[40] Jacobs, R., and Durbin, P., 2001, "Simulations of bypass transition," *Journal of Fluid Mechanics,* **428**, pp. 185–212.

[41] Zaki, T. A., 2013, "From streaks to spots and on to turbulence: exploring the dynamics of boundary layer transition," *Flow, turbulence and combustion,* **91**, pp. 451–473.

[42] Fang, Y., Zhao, Y., Waschkowski, F., Ooi, A. S., and Sandberg, R. D., 2023, "Toward more general turbulence models via multicase computational-fluid-dynamics-driven training," *AIAA Journal*, pp. 1–16.

APPENDIX A: SINGLE-CASE TRAINED MODELS' PERFORMANCE

The performance of all the single-case trained models is shown here.

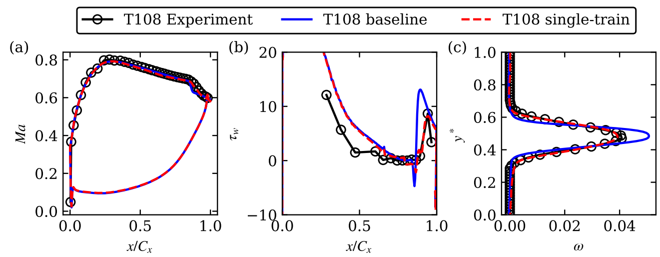

Fig. 12. Comparison of isotropic Mach number, wall shear stress and wake loss from the experiment, baseline, and single-case trained model for T108 case

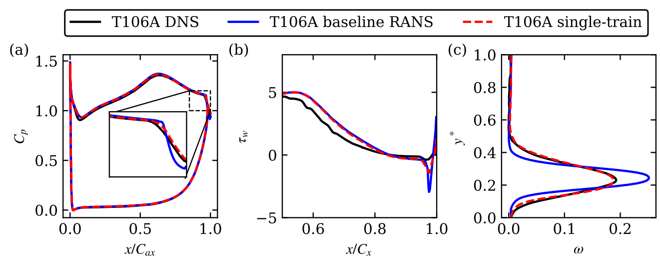

Fig. 13. Comparison on pressure coefficient, wall shear stress and wake loss from the experiment, baseline, and single-case trained model for T106A case

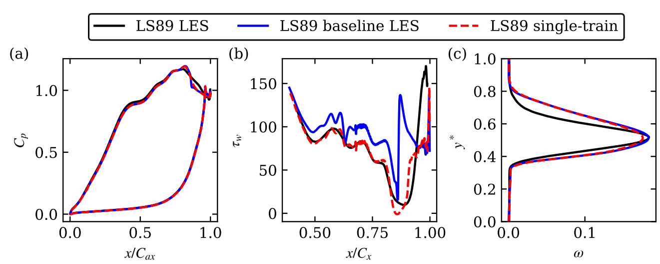

Fig. 14. Comparsion on pressure coefficient, wall shear stress and wake loss from the experiment, baseline, and single-case trained model for LS89 case

LIST OF FIGURES

This section will be created when figures are included with a caption.

LIST OF TABLES

This section will be created when tables are included with a caption.